

Article

# Microstructure Heredity of Inconel 718 Nickel-Based Superalloy during Preheating and Following Deformation

Jianguo Wang <sup>1,2,\*</sup>, Dong Liu <sup>1,2</sup>, Xiao Ding <sup>3</sup>, Haiping Wang <sup>1,2</sup>, Hai Wang <sup>1,2</sup>, Jingqing Chen <sup>1,2</sup> and Yanhui Yang <sup>1,2</sup>

<sup>1</sup> National Innovation Center of Defence Industry for Precise Forging and Ring Rolling, Northwestern Polytechnical University, Xi'an 710072, China; liudong@nwpu.edu.cn (D.L.); whp0604@mail.nwpu.edu.cn (H.W.); 17629268255@126.com (H.W.); chen13279352128@126.com (J.C.); yangyh@nwpu.edu.cn (Y.Y.)

<sup>2</sup> School of Materials Science and Engineering, Northwestern Polytechnical University, Xi'an 710072, China

<sup>3</sup> College of Chemistry and Chemical Engineering, Xianyang Normal University, Xianyang 712000, China; dingxiaolcu@126.com

\* Correspondence: jianguow@nwpu.edu.cn

Received: 13 February 2020; Accepted: 12 April 2020; Published: 15 April 2020



**Abstract:** Preheating and compression tests of Inconel 718 superalloy double cone specimens were carried out to investigate the microstructure heredity during hot working. Optical microscopy, scanning electron microscopy (SEM), electron backscatter diffraction (EBSD), and transmission electron microscopy (TEM) were used to characterize the microstructure evolution. The results show that intense microstructure heredity can be found at the temperature 960–990 °C. During the preheating process,  $\delta$  phase precipitation or grain growth could increase the fraction of high angle grain boundary (HAGBs) and  $\Sigma 3^n$  boundaries. Otherwise, the generation or spread of annealing twin could increase the fraction of LAGBs, Volume fraction of recrystallized grains was evaluated at the whole hot working process. At the temperature of 960–990 °C, the volume fraction of recrystallized grains increases with effective strain increasing. At the super solution temperature of  $\delta$  phase, the volume fraction of recrystallized grains decreases and then increases with the increase of the effective strain. The unimodal grain size distribution and fully recrystallized grains can be obtained at low strains at 960–990 °C. The twin boundary length fraction of deformed specimens is always lower than that of preheated ones. Discontinuous dynamic recrystallization (DDR<sub>X</sub>) was considered as the dominant nucleation mechanism, and continuous dynamic recrystallization (CDRX) was strengthened with the increasing grain size. Twin introduced deformation will be the main deformation mode for alloy 718 with larger grain.

**Keywords:** nickel-based superalloy; preheating; pouble cone compression; microstructure heredity

## 1. Introduction

Ni-based superalloys are widely used in propulsion components of the aerospace industry such as turbine engine blades, disks, casings, and liners. These alloys possess a desirable combination of high temperature strength and toughness, oxidation and creep resistance, and high temperature stability [1–3]. The strengthening mechanism of Inconel 718 alloy is mainly contributed by nano-scaled  $\gamma''$ -Ni<sub>3</sub>Nb precipitates (lens-like disc shape) and  $\gamma'$ -Ni<sub>3</sub>(AlTi) (cubic or spherical shape) [4]. Metastable  $\gamma''$  phases would transform to detrimental  $\delta$ -Ni<sub>3</sub>Nb phases during exposure above 650 °C [5,6]. It is important to control the thermomechanical processing (TMP) for obtaining the superior performance of Inconel 718. Microstructure evolution, including dynamic recrystallization and grain growth of Inconel 718, has been extensively studied during hot working [7–9] and post heating processes [2,10–12]. Owing

to the relatively low stacking fault energy of nickel-based superalloy, the recovery induced by dislocation climb and cross slip is weak [13]. Hence, recrystallization is one of the most significant mechanisms for microstructure evolution during hot working process. The recrystallization mechanism comprises the following three categories: dynamic recrystallization (DRX), meta-dynamic recrystallization (MDRX), and static recrystallization (SRX) [14]. Due to the difficulty of refining the grain size of superalloy by SRX, extensive studies have been conducted to investigate the dynamic recrystallization during hot working process [15–27]. It has been well accepted that the nucleation of dynamic recrystallization for superalloy includes discontinuous DRX (DDRX) and continuous DRX (CDRX)  $\delta$  phase shows clearly the pinning effect on the grain growth and stimulated the nucleation of dynamic recrystallization. Otherwise, few studies have been carried out to investigate microstructure evolution right after preheating which is more consistent with actual production.

The detailed investigation of microstructure evolution during TMP is usually conducted using isothermal tests based on uniaxial compression [2,28–30], uniaxial tensile [31,32], torsion [33–35], and plane strain compression [36–39]. Workpieces are firstly annealed to ensure the initial homogeneous microstructure [40]. Because of the sensitivity for microstructure evolution to the initial state [41], the derived information during preheating process is most pertinent to forging process. Semiatin [42] first conducted the double-cone compression tests of Waspaloy ingot material to evaluate the effect of different initial microstructure on deformation and dynamic recrystallization behavior. It reveals that the kinetics of dynamic recrystallization has been highly dependent on the initial state and hot working temperature. In the double-cone compression tests, strain locates at the high medium plane of the specimen and increases from edge to the center. Based on the above superiority, double cone compression enables the continuous observation of microstructure evolution with increasing strain, which avoids the difference of initial state.

In this study, the heating process and double-cone compression were conducted to investigate the microstructure heredity of Inconel 718 superalloy during whole hot deformation. Finite element method was also conducted to evaluate the effective strain of compressed specimens. Analyses of grain boundary misorientation were systematically carried out in order to investigate the effect of secondary phases, progress of DRX, evolution of twin boundary and grain size distribution. More attention was devoted to the nucleation of DRX and the deformation mechanism during hot deformation.

## 2. Experimental Procedures and Finite Element Model

### 2.1. Experimental Procedures

The materials used in the present work came from a 250 mm diameter Inconel 718 wrought billet. The chemical compositions (wt %) of Inconel 718 is as follows: Cr, 17.90; Ni, 53.88; Nb, 5.50; Mo, 3.12; Ti, 1.04; Al, 0.52; Co, 0.24; Cu, 0.065; C, 0.029; S, 0.0005; P, 0.10; Ta, <0.100, Fe, balances. Double cone specimens, having dimensions illustrated in Figure 1, were machined from the edge of billets. Compression tests were carried out in a servo hydraulic test system with load capacities 3150 KN, which comprised a pair of K403 superalloy dies with 252 mm in diameter and 75mm in height. The specimens were heated at the temperature from 960 to 1040 °C for 60 min to minimize the gradient of temperature and complete the microstructure evolution, and then compressed to a 60% height reduction at a speed of 10mm/s. Two dies are heated to 900 °C in order to minimize the die chilled region in the specimens. Before heating process, specimens were heated to 200 °C to spray glass lubricant on the surface to reduce the friction between specimens and dies. After forging, the specimens were quenched in water immediately in ten seconds.

Specimens after compression were sectioned longitudinally for microstructure analysis. The cut surfaces were mechanically polished and etched for optical metallographic and SEM examination. Specimens for EBSD investigation were machined and then polished electrolytically with 20 pct solution of H<sub>2</sub>SO<sub>4</sub> in methanol. Foils with the thickness of 300  $\mu$ m were prepared by grinding to a thickness of 60  $\mu$ m and discs with a diameter of 3 mm were cut from the selected location for TEM

examination. The discs were then twin-jet electropolished with a solution of 5% perchloric acid in ethanol at  $-30\text{ }^{\circ}\text{C}$ . Tecnai G2 F30 operated at 200 KV was performed for TEM analysis. SEM and EBSD studies were conducted on a VEGA TESCAN scanning electron microscope (TESCAN, Brno, Kohoutovice, Czech Republic) equipped with HKL channel 5 software (Oxford Instruments, Witney, Oxon, United Kingdom). Step size of 1–4  $\mu\text{m}$  and voltage of 20 KV were used.

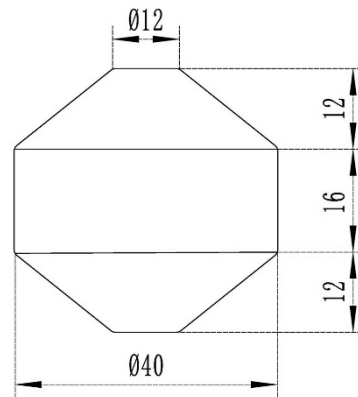


**Figure 1.** Dimensions of double cone specimens in millimeters.

## 2.2. Effective Strain Evaluation by FEM

Finite element model (showed in Figure 2) was used to evaluate effective strain of compressed specimens. Flow stress data of Inconel 718 generated by Gleeble-3500 at various temperatures and strain rate were used to simulate the deformation behavior of double cone specimens [42]. The geometry of specimens and dies, temperatures (including specimens, dies, and environment), and compression rate were consistent with experimental procedures. The heat transfer coefficient and specific heat increase with temperature as to the reference [43]. Friction coefficient (0.3) and heat transfer coefficient between specimen and dies were assumed to be constant during the hot deformation. Two dies were deemed as a rigid body in the FE model as to its deformation can be neglected compared with specimens. Calculations were done by using the commercial code of DEFORM-2D software (SFTC, V10.2, Columbus, OH, United States). Adiabatic temperature rise was estimated as to the equation shown in reference [44].

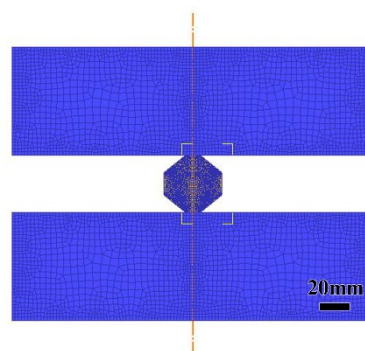


**Figure 2.** Finite element model of double cone compression tests.

## 3. Results and Discussion

### 3.1. Initial Microstructure

The initial microstructure of each specimen was detected, which reveals the fine uniform grains with a maximum grain size about 16  $\mu\text{m}$ . The microstructure of wrought billet can be seen in Figure 3. It shows the EBSD map of the microstructure which is composed of twin boundaries, low angle grain

boundary (LAGBs,  $2 \leq \theta \leq 15$ , thin black lines), high angle grain boundary (HAGBs,  $\theta > 15$ , thick black lines). The LAGBs can only be observed in few specific grains. The fraction of  $\Sigma 3$  twin boundaries is about 20%, and the fraction of  $\Sigma 3^n$  ( $n = 2, 3$ ) twin boundaries is lower than 2%.

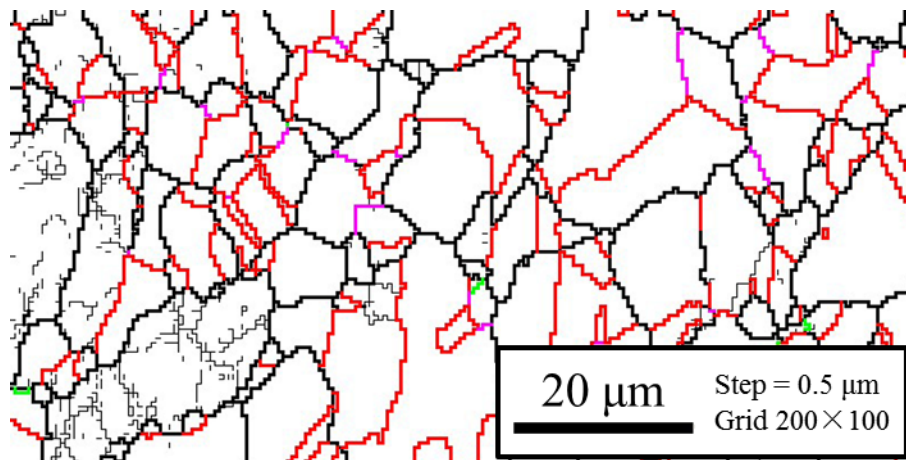


**Figure 3.** Initial microstructure of specimen: thin black lines represent the low angle grain boundary; thick black lines represent the high angle grain boundary; red, pink, green lines represent  $\Sigma 3$ ,  $\Sigma 9$ ,  $\Sigma 27$ , twin boundaries respectively.

### 3.2. Strain Distribution and Flow Behavior

The thermo-mechanical parameters of double cone specimen deformed at the temperature of 1010 °C are shown in Figure 4. It reveals that the effective strain increases from 0.2 at the edge to 1.6 at the center along the high middle plane (Figure 4a). The width of each zone for similar effective strain is about 3 mm which is sufficient for microstructure investigation. In order to investigate the flow behavior of double cone specimen during hot compression, the thermo-mechanical parameters evolution with strain increasing were picked-up at the three points as showed in Figure 4a. The evolution of effective stress and effective LnZ parameter with effective strain increasing were shown in Figure 4b. The Zener parameter was estimated by using the following equation [36]:

$$Z = \dot{\epsilon} \exp(Q/RT) \quad (1)$$

where  $\dot{\epsilon}$  is effective strain rate,  $Q$  is the activation energy for hot deformation (401.1 kJ/mol) which was calculated according to flow stress data [43],  $R$  is the gas constant (8.314 J/mol/k), and  $T$  is temperature in Kelvin. It can be found that the stress-strain curves for three points are comparable in peak stress and steady stress. With strain increasing, the effective stress increases to the peak and then decreases to the steady state, which is similar to the flow stress of cylindrical compression tests. According to the effective stress-effective strain curves, the effective strain of point 3 is higher than peak strain, which indicated the dynamic recrystallization starting; the effective strain of point 2 located at steady strain, which reveals the dynamic equilibrium between the working hardening and dynamic softening, while the effective strain of point 1 is much higher than steady strain represents the evolution of dynamic recrystallization. At the same time, it can be seen that the trend of curves is affected by the Zener parameters. The value of LnZ increases to a steady state of 36 with strain increasing. While the effective strain is higher than 0.8, the effective stress decreases again, which is due to the decreases of LnZ. As to the lower Zener parameter, the effective stress of point 2 is less than that of the other two points. The effect of Zener parameter on microstructure evolution will be neglected at specific heating temperature owing to its minute difference with increasing strain.

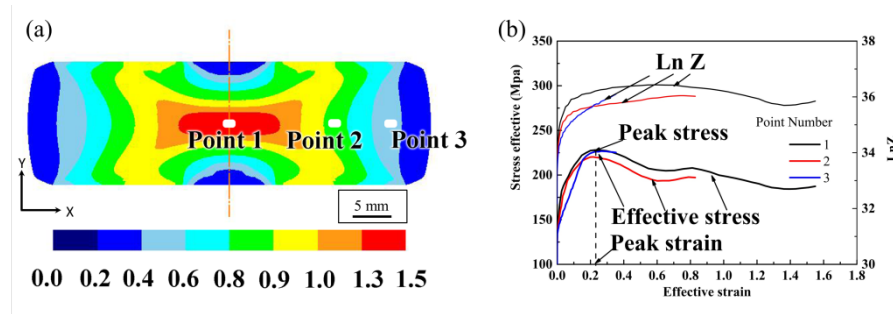


**Figure 4.** Thermo-mechanical parameters of double cone specimen compressed at 1010 °C. (a) Effective strain distribution at cross section, point 1, 2, 3 locates in the center, 1/2 radius and edge of specimen, respectively; (b) Effective stress and LnZ versus with effective strain of point 1, 2, 3 shown in (a).

### 3.3. Effect of Preheating Process on the Microstructure Evolution

The microstructure after the heating process will be the initial microstructure of hot compression tests owing to the sufficient heating time. Figure 5 shows the microstructure of specimens heated at different temperatures. The average grain size increases with temperature increasing, indicating the grain growth during heating process. Similar grain size (about 5.0  $\mu\text{m}$ ) can be found between the specimens heated at 960–990 °C (Figure 5a,b) and the initial state (Figure 3) which can be contributed to the pinning effect of  $\delta$  phases as discussed by Muralidharan [45]. Figure 6 shows the morphology of  $\delta$  phases after heated at 960 °C and 990 °C. The blocky  $\delta$  phases reside at the grain boundaries and intragranular, which hinders the grain growth. Smaller grains are also shown at the triple boundary (Figure 5a,b) which left from the initial state. Grain growth can be obviously observed at higher temperatures (Figure 5c,d) due to the higher grain boundary migration rate and lower pinning effect [46,47]. The average grain size is about 25  $\mu\text{m}$  (Figure 5c) and 60  $\mu\text{m}$  (Figure 5d) without regard for anneal twinning grains. At the same time, a mount of annealing twin can be found 1040 °C. This is consistent with the prior findings that the amount of annealing twin increasing with the increase of grain boundaries migration rate [48].

Misorientation angle distribution of the alloy heated at different temperatures were also shown in Figure 5. In other words, the frequency of LAGBs ( $2^\circ \leq \theta \leq 15^\circ$ ) and HAGBs have no clearly relation with temperature. Lower frequency of LAGBs was observed at the temperature of 960 °C and 1010 °C, and higher frequency of LAGBs was found at the temperature of 990 °C and 1040 °C. For low stacking fault energy alloys, the evolution of microstructure during the heating process can be ascribed to recovery, recrystallization, grain growth, and anneal twinning generation or spread [49]. Static recovery is considered as the main mechanism of microstructure evolution due to no obviously static recrystallization and grain growth observed at the temperature lower than 990 °C. Otherwise, the recovery rate of alloy at 960 °C is higher than that at 990 °C which is contrasted with the former results that the recovery rate increases with temperature increasing. It can be seen from Figure 6 that the volume fraction of  $\delta$  phases heated at 960 °C is higher than that heated at 990 °C. This can be connected to the precipitation of  $\delta$  phases which accelerated the transformation from LAGBs to HAGBs. At the temperature higher than 1010 °C, obvious grain growth can be observed, and it is responsible for the decreasing of LAGBs. A higher frequency of LAGBs at 1040 °C is contributed to the annealing twin generation and growth since LAGBs can be observed besides anneal twinings (Figure 5d).

It also can be seen that the fraction of  $\Sigma 3$  boundaries decreases first and then increases with temperature increasing. It should be noticed that three mainly ways are responsible for the generation of  $\Sigma 3$  boundaries. The first way is the static recrystallization and grain growth during the heating process, the second way is the generation and growth of anneal twinning, and the third way is the interaction between pre-existing  $\Sigma 3$  boundaries through grain boundary migration [50]. Due to the similar grain size, the fraction decreasing of  $\Sigma 3$  boundaries at 960–990 °C can be contributed to precipitation of  $\delta$  phases. The increase of  $\Sigma 3$  boundary fraction at the temperatures from 1010 °C to

1040 °C can be attributed to grain growth and anneal twinning. At the same time, the fraction of  $\Sigma 9$  boundary decreases slightly and the fraction of  $\Sigma 27$  boundary increases slightly with increasing temperature. This indicated that the interaction between pre-existing  $\Sigma 3^n$  boundary has a slight influence on the fraction of twinning boundaries.

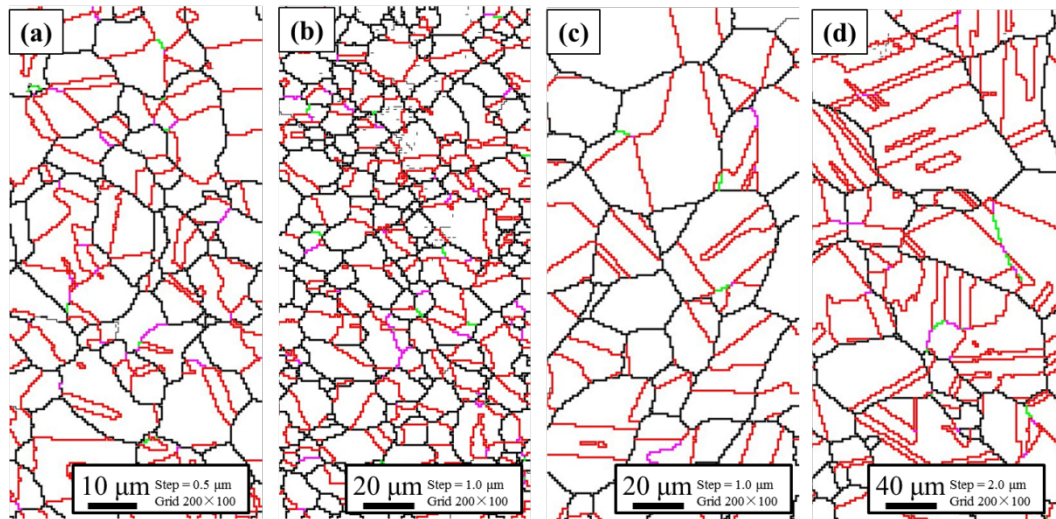


**Figure 5.** Grain boundary maps of specimens heated at different temperatures: (a) 960 °C, (b) 990 °C, (c) 1010 °C, (d) 1040 °C (Thin black lines represent the low angle grain boundary; thick black lines represent the high angle grain boundary; red, pink, green lines represent  $\Sigma 3$ ,  $\Sigma 9$ ,  $\Sigma 27$ , twin boundaries respectively).

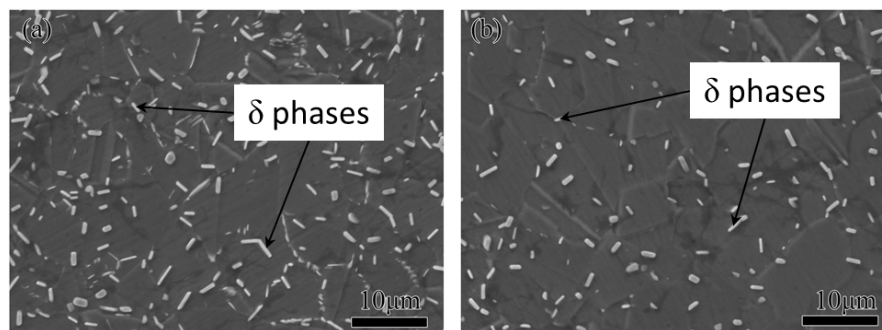


**Figure 6.** SEM image (secondary electronic signal) of  $\delta$  phases [5] in the specimens heated at 960 °C (a) and 990 °C (b).

### 3.4. Microstructure Evolution during Compression

Figure 7 shows the grain boundary maps of the alloy deformed to a 0.4 effective strain with different temperatures. Obviously, nucleation mechanisms, the volume fraction of DRX grains, and the average grain size are highly influenced by the temperature. Due to the effective strain has exceeded peak strain, the dynamic recrystallization has started, and the nucleation can be observed at the bulging grain boundary and interior of original grains. This indicated that DDRX (discontinuous dynamic recrystallization) and CDRX (continuous dynamic recrystallization) are both responsible for the nucleation of DRX [51,52]. With the increasing temperature, the large size of DRX grains reveals the high migration rate of grain boundary. The volume fraction of DRX grains is evidently low at the temperature of 1040 °C, indicating a lower nucleation rate which can be attributed to the grain growth during the preheating process.

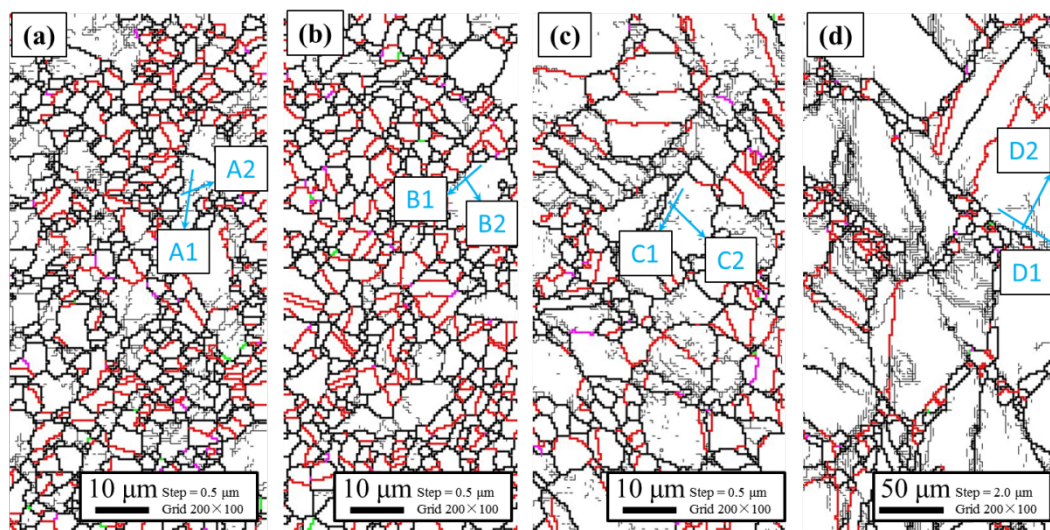


**Figure 7.** Grain boundary maps of the specimens deformed to a 0.4 effective strain with different temperatures (Thin black lines represent the low angle grain boundary; thick black lines represent the high angle grain boundary; red, pink, green lines represent  $\Sigma 3$ ,  $\Sigma 9$ ,  $\Sigma 27$ , twin boundaries respectively, A1, A2, B1, B2, C1, C2, D1, D2 were marked to analyses the misorientation within grains in Section 3.4.5.): (a) 960 °C, (b) 990 °C, (c) 1010 °C, (d) 1040 °C.

### 3.4.1. Volume Fraction of Recrystallized, Substructure and Deformed Grains

In order to calculate the volume fraction of recrystallization, the recrystallized grains have to be distinguished precisely from the substructured and deformed-grains. Zhang et al. distinguished recrystallized grains by analysis the grain orientation spread (GOS), which is defined as the average difference in orientation between all measurement within a single grain [16]. The GOS value of the recrystallized grains is lower than that of the substructure and deformed grains. Volume fraction of recrystallized grains can be obtained accurately by analysis the EBSD data since no strain and step size dependence for GOS value. Grains with a GOS value less than  $2^\circ$  are considered as recrystallized grains [16]. Figure 8 shows the GOS distribution of the alloy after heated at 1040 °C and deformed to a 0.4 effective strain. It can be noted that the GOS distribution of alloy after heated is multimodal. GOS distribution of alloy deformed to 0.4 effective strain exhibits only one prominent peak approximately up to  $7^\circ$ , which matches well with the first two peaks of the heated specimen. In this study, grains with GOS value from  $2\sim 7.5^\circ$  are considered as substructured grains, and the grains with GOS value higher than  $7.5^\circ$  are defined as deformed grains. Figure 9 shows the EBSD maps of alloy deformed to at 1040 °C for 0.4 effective strain. The recrystallized grains, substructure and deformed grains are featured by blue, yellow and red colors, respectively. Obviously, the recrystallized grains and substructure grains can be easily characterized. The volume fraction of DRX and substructured grains is about 12% and 15%.

Based on the GOS approach, the volume fraction of recrystallized, substructured, and deformed grains are shown in Figure 10, with the zero effective strain acquired at the specimens after the preheating process. At the temperature of 960~990 °C (Figure 10a,b), it can be found that the volume fraction of recrystallized grain increases with effective strain increasing. Otherwise, with effective strain increasing, the volume fraction of recrystallized grains decreases first and then increases while deformation conducted at 1010~1040 °C (Figure 10c,d). The completely recrystallization can only be found in the specimen after preheated at 1010 °C, and the highest volume fraction of DRX during deformation is about 80%. The lower recrystallization fraction of specimens after heated at the temperature lower than 990 °C can be contributed to the pinning effect of  $\delta$  phases which arrests the grain boundary and retrains the static recrystallization. The volume fraction of recrystallization for heated specimens increases and then decreases with the increasing temperature. The lower recrystallization fraction

observed in specimen after heating at 1040 °C can be attributed to annealing twins generated and growth, as discussed in Section 3.2.

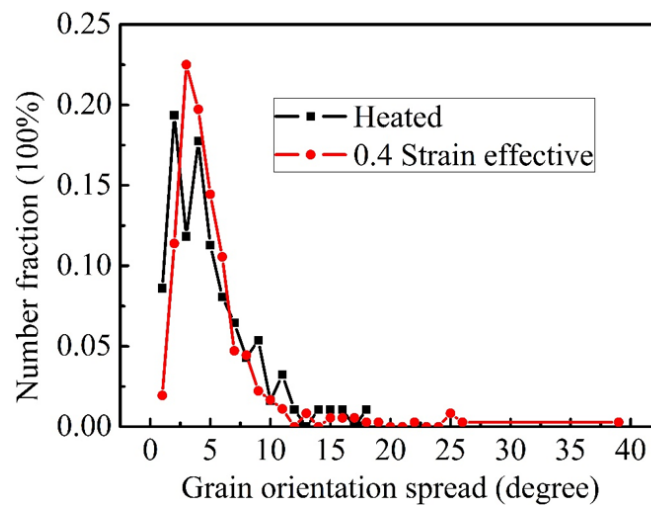


**Figure 8.** GOS distribution of the specimens after heated at 1040 °C and deformed to a 0.4 effective strain.

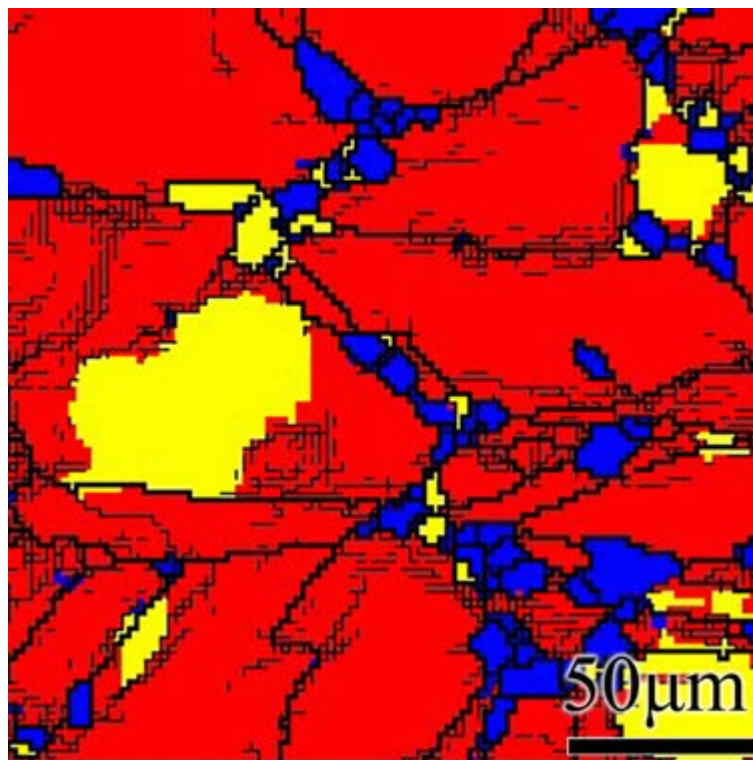


**Figure 9.** Microstructure of the specimens deformed to a 0.4 effective strain at 1040 °C (red, yellow, blue represent deformed, sub-structured and recrystallized grains respectively).

A noticeable difference can also be observed on the volume fraction of substructured grains (Figure 10). This indicated that the substructured grains obtained by the heating process have a significant influence on the evolution of dynamic recrystallization. Otherwise, the volume fraction of substructured grains remains steady at the strain range of 0.4~1.5, indicating that the strain has a slight effect on the volume fraction of substructure grains under special Zener parameters. Moreover, the steady value of substructure grains during deformation shows clear evidence of the CDRX which is consistent with the investigation of former researchers [18].

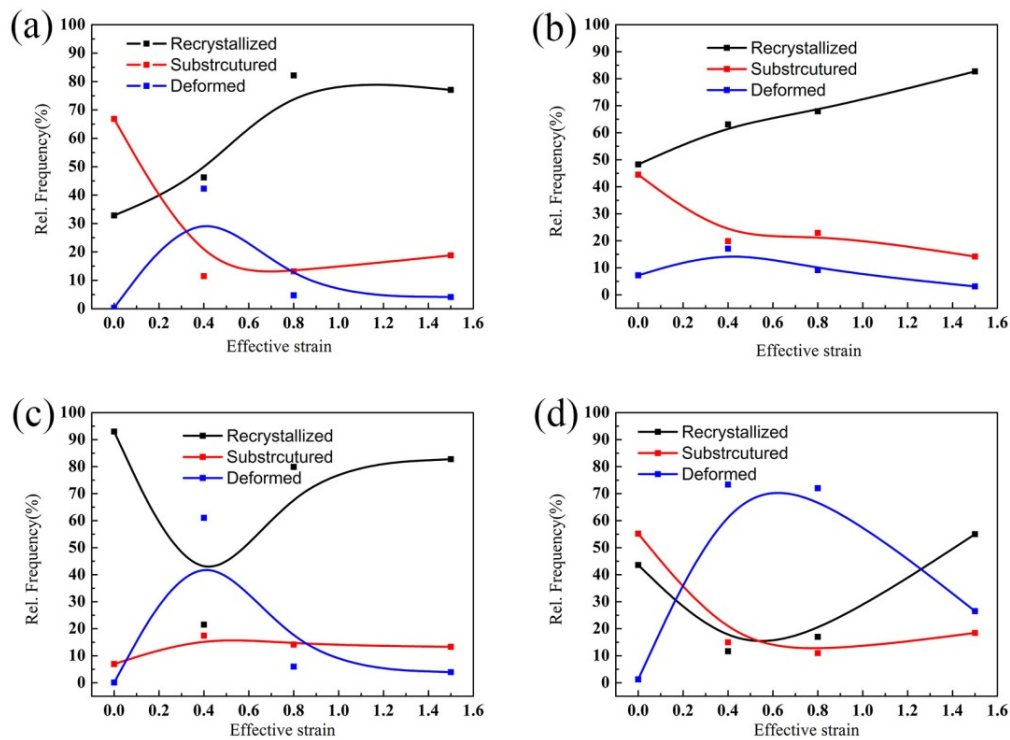


**Figure 10.** Volume fraction of DRX grains, substructure grains and deformed grains at: (a) 960 °C, (b) 990 °C, (c) 1010 °C, (d) 1040 °C.

The difference of volume fraction for three types grains (recrystallized, substructured and deformed) reveals the transformation among recrystallized, substructure and deformed grains. It can be found that the temperature has a distinct influence on the microstructure evolution during the beginning of hot deformation. At the temperature of 960 °C and 990 °C (Figure 10a,b), the volume fraction of substructured grains decreases as the fraction of recrystallized and deformed grains increases. At 1010 °C (Figure 10c), the volume fraction of recrystallized grains decreases, and the fraction of substructure and deformed grains increases. At 1040 °C (Figure 10d), the volume fraction of recrystallized and substructure grains decreases, and the deformed grains increases. Based on the above analysis, the substructured grains can translate to recrystallized grains immediately at temperatures lower than 990 °C. Otherwise, substructured grains translate to deformed grains first and then recrystallized with strain increasing at higher temperatures. It also indicated that the substructured grains accelerate the dynamic recrystallization at lower temperature.

Volume fraction of deformed grains increases first and then decreases with strain increasing (Figure 10). The increasing of deformed grains has always been considered as the increasing of dislocation density, and the decreasing of deformed grains can be contributed to the evolution of DRX which is considered as the main soften mechanism for Nickel based alloy. While the volume fraction of recrystallized grains is steady, the volume fraction of deformed grains holds steady with a value lower than 5% (Figure 10c,d). When the volume fraction of recrystallized grains is higher than 50% (Figure 10a–c), the fraction of substructure grains is higher than that of deformed grains. This indicated that few of recrystallized grains could transfer to substructure grains while the volume fraction of recrystallized grain is higher than 50% at the temperature lower than 1010 °C. However, at the temperature of 1040 °C (Figure 10d), the fraction of deformed grains is always higher than that of substructure grains, indicating that higher misorientation can be obtained at recrystallized grains while deformed at higher temperatures.

### 3.4.2. Misorientation Angle Distribution

Figure 11 shows the misorientation angle distributions of specimens deformed at different temperatures. At the temperature of 960, 1010, and 1040 °C (Figure 11a,c,d), the fraction of grain

boundary with misorientation 0~5 and 5~15° increases first and then decreases with increasing strain. Otherwise, the fraction of HAGBs decreases first and then increases with strain increasing. At low effective strains, HAGBs generated during preheating process transfer to LAGBs leads to the increasing of LAGBs fraction. At higher effective strain, the increasing of HAGBs fraction can be contributed to the nucleation and growth of DRX grains which reduce the dislocation density and substructure fraction. At the temperature of 990 °C (Figure 11b), fraction of grain boundary with misorientation 0~5° decreases with effective strain increasing, the fraction of grain boundary with misorientation 5~15° increases first and then hold steady. The fraction of HAGBs increases with effective strain increasing. This indicated that LAGBs transfer HAGBs which activates the DRX at the beginning of deformation during deformed at 990 °C.

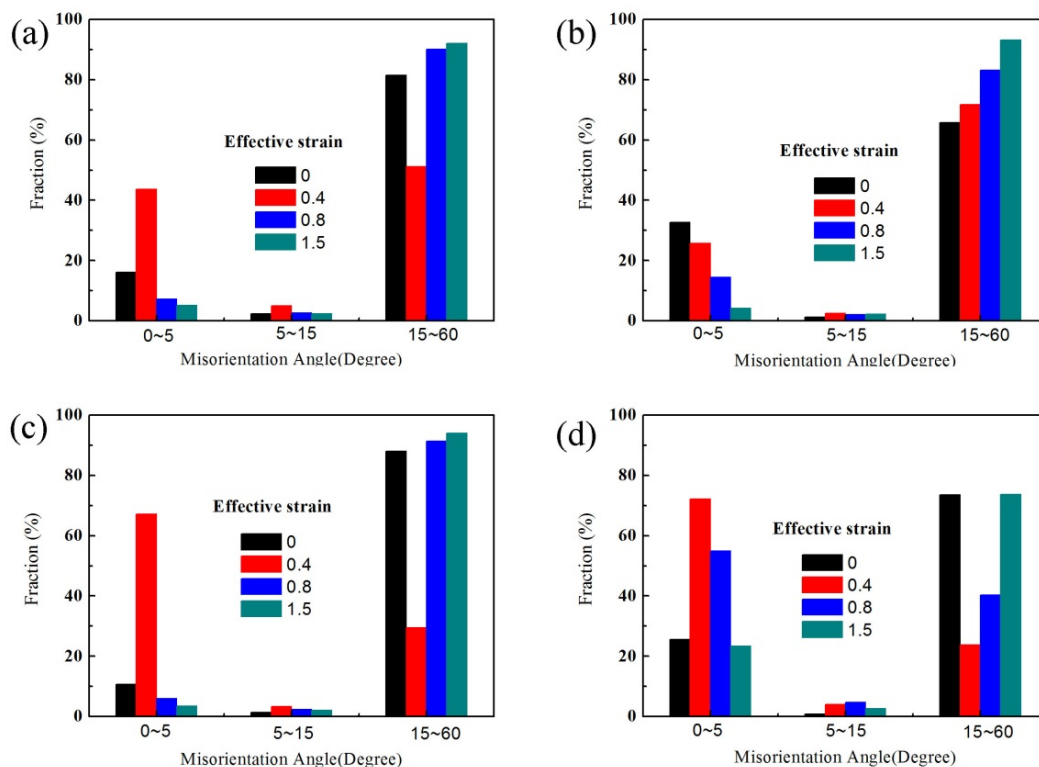


**Figure 11.** Misorientation angle distribution of the deformed alloy at: (a) 960 °C, (b) 990 °C, (c) 1010 °C, (d) 1040 °C.

While the effective strain is exceeded to 0.8 at the temperature lower than 1010 °C, the frequency of HAGBs is higher than 80%, and the peak frequency of grain boundary with misorientation 5~15° was found at an effective strain of 0.4. However, the frequency of HAGBs is about 40.3% under a strain of 0.8 at 1040 °C, and the peak frequency of grain boundary with misorientation 5~15° was found at the effective strain of 0.8. This is consistent with the kinetics of dynamic recrystallization as shown in Figure 10.

### 3.4.3. Grain size Distribution

In order to obtain excellent properties, fine grains and a uniform microstructure must be achieved through the deformation process. The grain size distribution of specimens after heating and deformation at different temperatures are shown in Figure 12. The smallest step size of respectively pixel size of the raw data is 0.5  $\mu\text{m}$ . Multimodal grain diameter distribution can be found in specimens heated at all temperatures. The number of peaks increases with temperature increasing indicated that the uniformity of microstructure decreases with temperature increasing. With effective strain increasing, the grain size distribution changes from multimodal to unimodal indicating the DRX increases the uniformity of

microstructure. While effective strain is greater than 0.8, the effective strain has slight influence on the grain diameter distribution. At the temperature of 1010 °C and 1040 °C (Figure 12c,d), the fraction of DRX grains increase with the increase of effective strain. And the unimodal grain diameter distribution only obtained at the effective strain of 1.5 at 1010 °C. The microstructure of specimen deformed at 1010 °C and an effective strain of 1.5 is shown in Figure 13a. It can be observed that the microstructure is composed by equiaxed grains indicating the fully completion of DRX. Otherwise, multimodal grain diameter distribution returns at an effective strain of 1.5 with the temperature increased to 1040 °C (Figure 12d), as shown in Figure 13b. This can be attributed to the larger grain size grew at the preheating process under 1040 °C.

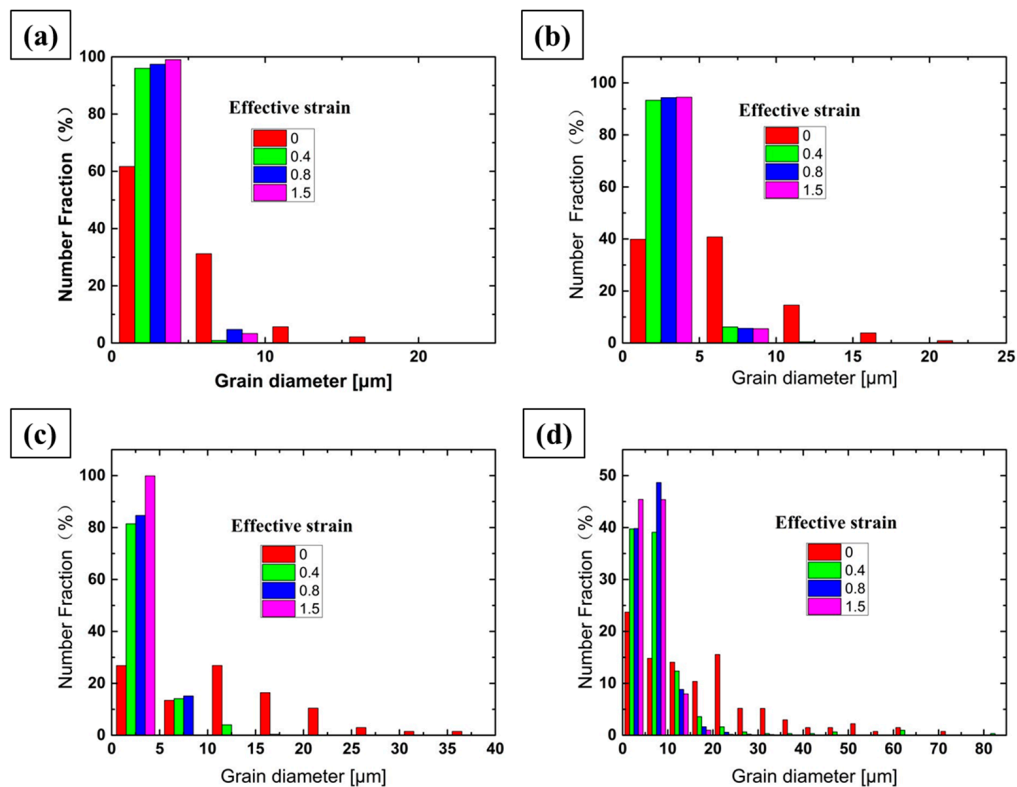


**Figure 12.** Grain size distribution of the heated and deformed specimens at: (a) 960 °C, (b) 990 °C, (c) 1010 °C, (d) 1040 °C.

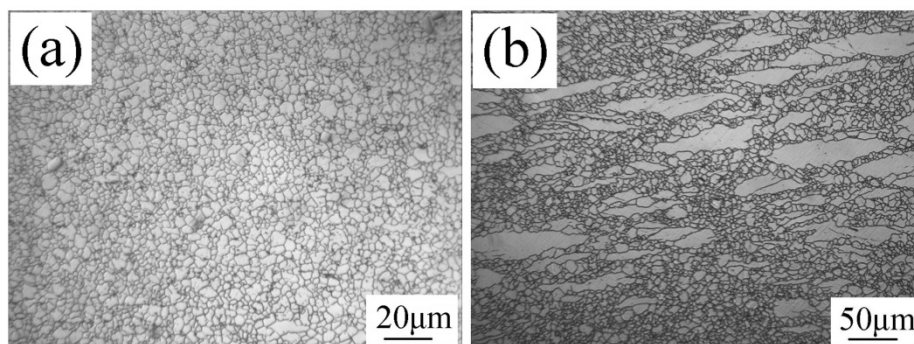


**Figure 13.** OIM of microstructure with an effective strain of 1.5: (a) 1010 °C, (b) 1040 °C.

#### 3.4.4. Twinning Grain Boundary

The fraction of  $\Sigma 3^n$  ( $n = 1, 2, 3$ ) twin boundary during hot working is shown in Figure 14. It can be observed that the fraction of  $\Sigma 3$  twin boundary decreases first and then increases to a stable value

with effective strain increasing. Compared with Figure 11, it is indicated that the fraction of  $\Sigma 3^n$  ( $n = 1, 2, 3$ ) twin boundary increases with the DRX grains fraction increasing which is consistent with Zhang [16]. The stable value of  $\Sigma 3$ ,  $\Sigma 9$ ,  $\Sigma 27$  is about 20%, 1%, and 0.2% with no obvious connection with temperature. Moreover, it is much lower than the value after heating process, indicating that it is more effective to increase the fraction of  $\Sigma 3$  twin boundary by heating process. While deformed at 1040 °C, the fraction of  $\Sigma 3$ ,  $\Sigma 9$  twin boundary is lower than other temperatures due to the lower nucleation rate at the boundary of grew grain. The  $\Sigma 3$  twin boundary generated during heating process lost their twin characteristics at the beginning of deformation leads to the decreasing of  $\Sigma 3$  twin boundary fraction. This can be attributed to the accumulation of dislocation at the twin boundary which changes the orientation of twins. At 990 °C, the fraction of  $\Sigma 3$  twin boundary changes slightly during hot processing, and the stable value can be obtained at a lower effective strain than at other temperatures. Thus, hot working should be performed at 990 °C in order to obtain a high fraction of  $\Sigma 3$  twin boundary.

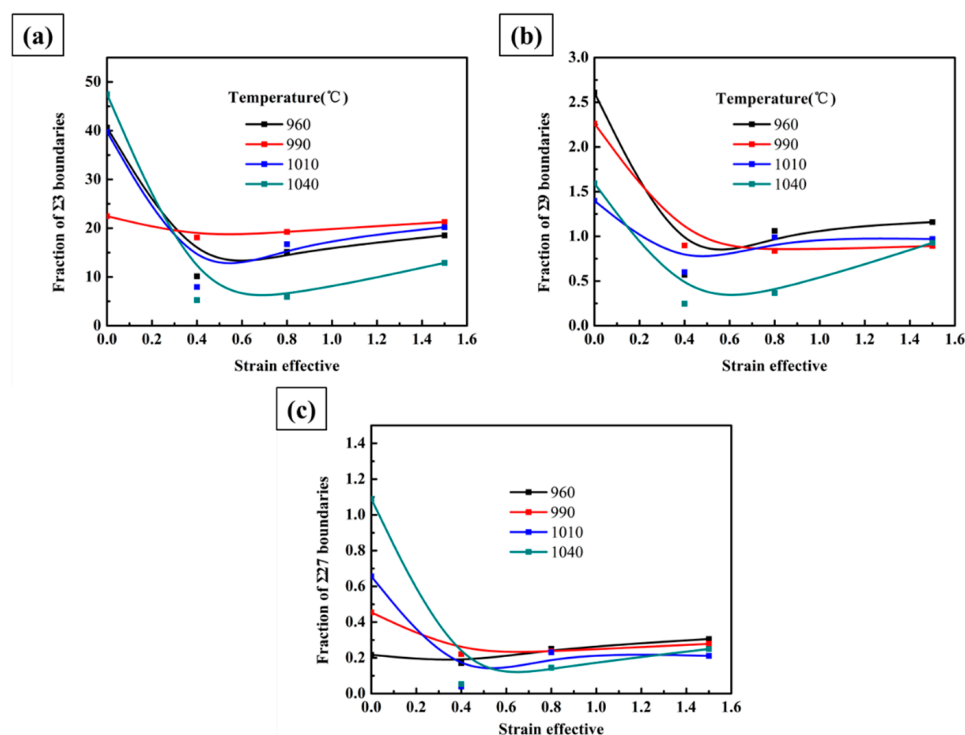


**Figure 14.** The evolution of twin boundary fraction: (a)  $\Sigma 3$  boundary; (b)  $\Sigma 9$  boundary; (c)  $\Sigma 27$  boundary.

### 3.4.5. Effect of Temperature on the Deformation Mechanism

Figure 15 shows the misorientations measured along the lines marked in Figure 7. It can be seen that the temperature has obviously influence on the deformation mechanism. At the temperature of 960 °C, the point-to-origin misorientations (cumulative misorientations) [46] can exceed 10° near the original grain boundaries, but are lower than 5° within the grains, as shown in Figure 15a,b, implying that the misorientation accumulates has been well developed near the grain boundaries. The cumulative misorientations show a large orientation gradient along the original grain boundaries which can accumulate adequate misorientation to nucleation and transfer to HAGBs. It also reveals that the bulging of grain boundaries can be considered as the main mechanism of nucleation. As showed in Figure 15c,d, the cumulative misorientations can hardly exceed 7° at the temperature of 990 °C, reveals the lower orientations gradient and store energy. It can be confirmed that the stored energy is much higher in the alloy deformed at low temperature. At 960 °C, the driving force needed for nucleation is much higher due to the strong pinning effect of  $\delta$  phases. As shown in Figure 16, dislocation accumulation along the boundaries increases the orientation gradient and the nucleation rate.

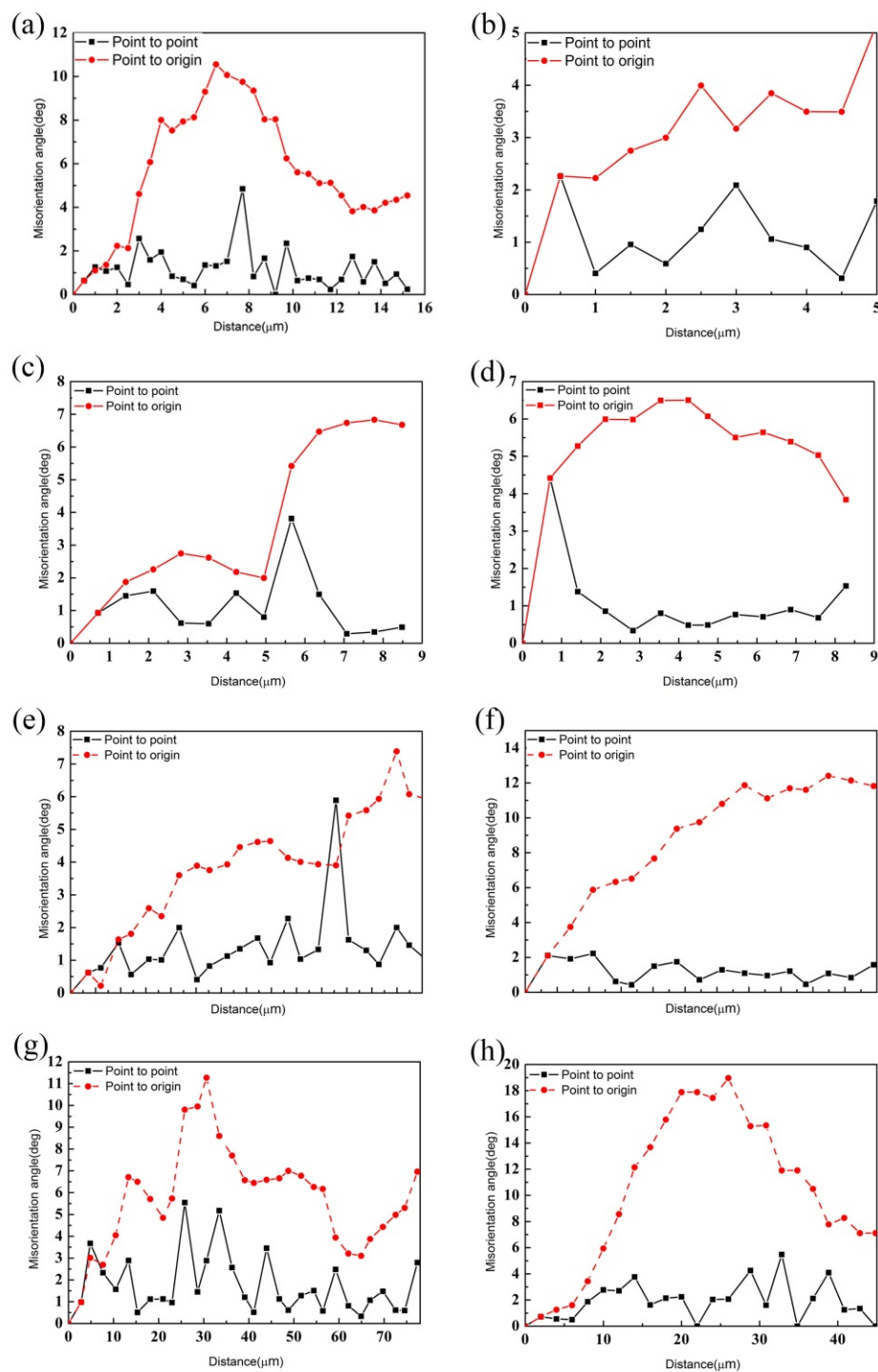


**Figure 15.** Misorientations measured along the lines marked in Figure 7: (a) A1, (b) A2, (c) B1, (d) B2, (e) C1, (f) C2, (g) D1, (h) D2.

Figure 15e,f shows that the point-to-origin misorientations can exceed  $10^\circ$  within the grains at  $1010^\circ\text{C}$ . At the same time, the cumulative misorientations can easily exceed  $10^\circ$  both along the boundary and intragranular, as shown in Figure 15g,h. This implies that the misorientations accumulation has been well developed within the grains at the temperature higher than  $1010^\circ\text{C}$ . The effect of temperature on the interface energy and stacking fault energy can be neglected at  $960\sim 1040^\circ\text{C}$ . The main reason for the misorientation accumulation can be attributed to the larger grain size at the high temperature. As shown in Figure 7d, it can be seen that the LAGBs within the grains parallel to each other. The TEM

image of specimen deformed at 1040 °C is shown in Figure 17, and amount of deformation twin can be observed. It can be concluded that the twin introduced deformation can be considered as the main deformation mechanism of alloy at 1040 °C. The deformation behavior is affected by stacking fault energy and grain size [53]. It is well accepted that the deformation twin will be more usual with an increase of the stacking fault energy and grain size. In this study, the grain size can be considered as the main reason for the evolution of the deformation mechanism.



Figure 16. TEM image of specimen deformed at 960 °C.

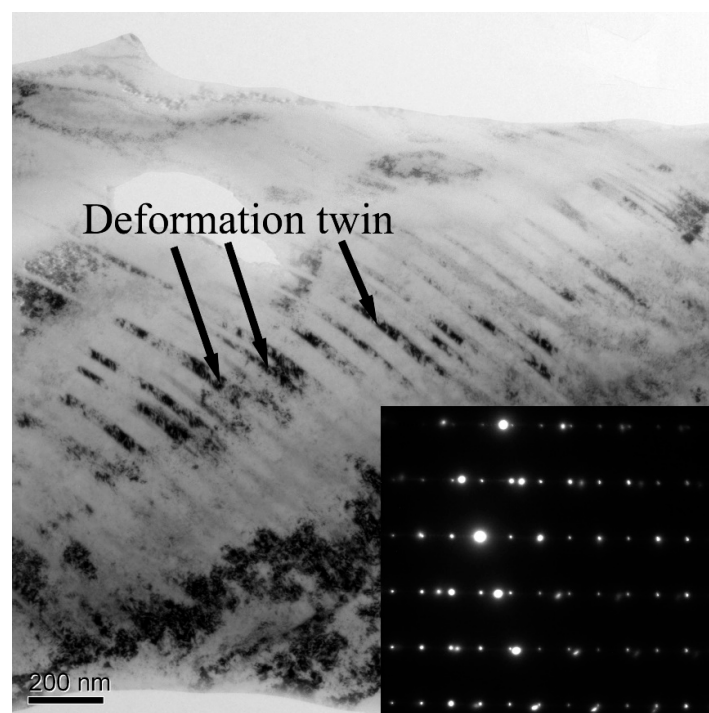


Figure 17. TEM image of specimen deformed at 1040 °C.

#### 4. Conclusions

Double cone compressions were carried out on Nickel based superalloy to investigate the effect of temperature on the microstructure heredity during heating and following the deformation process. From the above analysis, the results can be concluded:

- (1) A continuous, increased effective strain can be obtained by double cone compressions, which is more convenient to investigate the microstructure heredity during hot deformation from zero to high strains.
- (2) Intense microstructure heredity can be found at 960~990 °C, which is much lower than the temperature needed for the dissolution of  $\delta$  phases.
- (3) At the temperature lower than 990 °C, the volume fraction of recrystallized grain increases with effective strain increasing. At higher temperatures, the volume fraction of recrystallized grain decreases and then increases with the increase of effective strain. The unimodal grain diameter distribution can be obtained at lower strains at the low temperature. The fraction of twin boundaries decreases first and then increases with effective strain increasing.
- (4) The nucleation mechanism of DDRX and CDRX occurred simultaneously in the alloy during hot deformation, which was closely related to the grain size after the heating process. It was noted that CDRX was strengthened with the increase of grain size. The twin introduced deformation will be the primary deformation mode for alloys with a larger initial grain size.

**Author Contributions:** Data curation, H.W. (Haiping Wang) and J.C.; Formal analysis, H.W. (Hai Wang); Funding acquisition, Y.Y.; Investigation, J.W.; Methodology, D.L.; Software, X.D. All authors have read and agreed to the published version of the manuscript.

**Funding:** This research was funded by Fundamental Research Funds for the Central Universities (No.3102019ZX004) and Natural Science Foundation of Shaanxi Province, China (2020JQ-182).

**Conflicts of Interest:** The authors declare no conflict of interest.

#### References

1. Luo, Z.J.; Liu, D. Evaluation of IN718 disk-forging processes using the quality-loss function. *J. Mater. Process. Technol.* **1996**, *59*, 381–385. [[CrossRef](#)]
2. Wei, X.; Zheng, W.; Song, Z.; Lei, T.; Yong, Q.; Xie, Q. Static recrystallization behavior of Inconel 718 alloy during thermal deformation. *J. Wuhan Univ. Technol.-Mater. Sci. Ed.* **2014**, *29*, 379–383. [[CrossRef](#)]
3. Araujo, L.S.; Santos, D.S.D.; Godet, S.; Dille, J.; Pinto, A.L.; de Almeida, L.H. Analysis of Grain Boundary Character in a Fine-Grained Nickel-Based Superalloy 718. *J. Mater. Eng. Perform.* **2014**, *23*, 4130–4135. [[CrossRef](#)]
4. Li, R.B.; Yao, M.; Liu, W.C.; He, X.C. Isolation and determination for  $\delta$ ,  $\gamma'$  and  $\gamma''$  phases in Inconel 718 alloy. *Scr. Mater.* **2002**, *46*, 635–638. [[CrossRef](#)]
5. Sundararaman, M.; Mukhopadhyay, P.; Banerjee, S. Some aspects of the precipitation of metastable intermetallic phases in INCONEL 718. *Metall. Trans. A* **1992**, *23*, 2015–2028. [[CrossRef](#)]
6. Devaux, A.; Eacute, L.N.; Molins, R.; Pineau, A.; Organista, A.; Guédou, J.Y.; Uginet, J.F.; Eacute, P.H. Gamma double prime precipitation kinetic in Alloy 718. *Mater. Sci. Eng. A* **2008**, *486*, 117–122. [[CrossRef](#)]
7. Thomas, A.; El-Wahabi, M.; Cabrera, J.M.; Prado, J.M. High temperature deformation of Inconel 718. *J. Mater. Process. Technol.* **2006**, *177*, 469–472. [[CrossRef](#)]
8. Medeiros, S.C.; Prasad, Y.V.R.K.; Frazier, W.G.; Srinivasan, R. Microstructural modeling of metadynamic recrystallization in hot working of IN 718 superalloy. *Mater. Sci. Eng. A* **2000**, *293*, 198–207. [[CrossRef](#)]
9. Nayan, N.; Gurao, N.P.; Murty, S.V.S.N.; Jha, A.K.; Pant, B.; George, K.M. Microstructure and micro-texture evolution during large strain deformation of Inconel alloy IN718. *Mater. Charact.* **2015**, *110*, 236–241. [[CrossRef](#)]
10. Deng, D.; Wang, C.; Liu, Q.; Niu, T. Effect of standard heat treatment on microstructure and properties of borided Inconel 718. *Trans. Nonferrous Metals Soc. China* **2015**, *25*, 437–443. [[CrossRef](#)]
11. Etas, P.J.P.K.; Osorio, L.A.R.; Mata, M.P.G.; Garza, M.D.L.; López, V.P. Influence of the Delta Phase in the Microstructure of the Inconel 718 subjected to “Delta-processing” Heat Treatment and Hot Deformed. *Procedia Mater. Sci.* **2015**, *8*, 1160–1165.

12. Zouari, M.; Bozzolo, N.; Loge, R.E. Mean field modelling of dynamic and post-dynamic recrystallization during hot deformation of Inconel 718 in the absence of  $\delta$  phase particles. *Mater. Sci. Eng. A* **2016**, *655*, 408–424. [[CrossRef](#)]
13. Lin, Y.C.; Wu, X.; Chen, X.; Chen, J.; Wen, D.; Zhang, J.; Li, L. EBSD study of a hot deformed nickel-based superalloy. *J. Alloys Comp.* **2015**, *640*, 101–113. [[CrossRef](#)]
14. Makower, H.; Skurska, Z. Mater. In *Recrystallization and Related Annealing Phenomena*; Elsevier: Amsterdam, The Netherlands, 1995; pp. 219–224.
15. Wen, D.; Lin, Y.C.; Li, H.; Chen, X.; Deng, J.; Li, L. Hot deformation behavior and processing map of a typical Ni-based superalloy. *Mater. Sci. Eng. A* **2014**, *591*, 183–192. [[CrossRef](#)]
16. Zhang, H.; Zhang, K.; Zhou, H.; Lu, Z.; Zhao, C.; Yang, X. Effect of strain rate on microstructure evolution of a nickel-based superalloy during hot deformation. *Mater. Des.* **2015**, *80*, 51–62. [[CrossRef](#)]
17. Zhang, H.; Zhang, K.; Lu, Z.; Zhao, C.; Yang, X. Hot deformation behavior and processing map of a  $\gamma'$ -hardened nickel-based superalloy. *Mater. Sci. Eng. A* **2014**, *604*, 1–8. [[CrossRef](#)]
18. Zhang, H.; Zhang, K.; Jiang, S.; Zhou, H.; Zhao, C.; Yang, X. Dynamic recrystallization behavior of a  $\gamma'$ -hardened nickel-based superalloy during hot deformation. *J. Alloys Comp.* **2015**, *623*, 374–385. [[CrossRef](#)]
19. Yu, Q.Y.; Yao, Z.H.; Dong, J.X. Deformation and recrystallization behavior of a coarse-grain, nickel-base superalloy Udimet720Li ingot material. *Mater. Charact.* **2015**, *107*, 398–410. [[CrossRef](#)]
20. Wang, J.; Dong, J.; Zhang, M.; Xie, X. Hot working characteristics of nickel-base superalloy 740H during compression. *Mater. Sci. Eng. A* **2013**, *566*, 61–70. [[CrossRef](#)]
21. Ning, Y.; Yao, Z.; Li, H.; Guo, H.; Tao, Y.; Zhang, Y. High temperature deformation behavior of hot isostatically pressed P/M FGH4096 superalloy. *Mater. Sci. Eng. A* **2010**, *527*, 961–966. [[CrossRef](#)]
22. Liu, Y.; Hu, R.; Li, J.; Kou, H.; Li, H.; Chang, H.; Fu, H. Characterization of hot deformation behavior of Haynes230 by using processing maps. *J. Mater. Process. Technol.* **2009**, *209*, 4020–4026. [[CrossRef](#)]
23. He, D.; Lin, Y.C.; Chen, M.; Chen, J.; Wen, D.; Chen, X. Effect of pre-treatment on hot deformation behavior and processing map of an aged nickel-based superalloy. *J. Alloys Comp.* **2015**, *649*, 1075–1084. [[CrossRef](#)]
24. Detrois, M.; Helmink, R.C.; Tin, S. Hot deformation characteristics of a polycrystalline  $\gamma$ - $\gamma'$ - $\delta$  ternary eutectic Ni-base superalloy. *Mater. Sci. Eng. A* **2013**, *586*, 236–244. [[CrossRef](#)]
25. Zhang, P.; Hu, C.; Ding, C.G.; Zhu, Q.; Qin, H.Y. Plastic deformation behavior and processing maps of a Ni-based superalloy. *Mater. Des.* **2015**, *65*, 575–584. [[CrossRef](#)]
26. Huang, L.; Qi, F.; Hua, P.; Yu, L.; Liu, F.; Sun, W.; Hu, Z. Discontinuous Dynamic Recrystallization of Inconel 718 Superalloy during the Superplastic Deformation. *Metall. Mater. Trans. A* **2015**, *46*, 4276–4285. [[CrossRef](#)]
27. Wang, Y.; Shao, W.Z.; Zhen, L.; Zhang, X.M. Microstructure evolution during dynamic recrystallization of hot deformed superalloy 718. *Mater. Sci. Eng. A* **2008**, *486*, 321–332. [[CrossRef](#)]
28. Zhang, J.M.; Gao, Z.Y.; Zhuang, J.Y.; Zhong, Z.Y.; Janschek, P. Strain-rate hardening behavior of superalloy IN718. *J. Mater. Process. Technol.* **1997**, *70*, 252–257. [[CrossRef](#)]
29. Wang, Y.; Zhen, L.; Shao, W.Z.; Yang, L.; Zhang, X.M. Hot working characteristics and dynamic recrystallization of delta-processed superalloy 718. *J. Alloys Comp.* **2009**, *474*, 341–346. [[CrossRef](#)]
30. Mandal, S.; Bhaduri, A.K.; Sarma, V.S. A Study on Microstructural Evolution and Dynamic Recrystallization during Isothermal Deformation of a Ti-Modified Austenitic Stainless Steel. *Metall. Mater. Trans. A* **2011**, *42*, 1062–1072. [[CrossRef](#)]
31. Hrutkay, K.; Kaoumi, D. Tensile deformation behavior of a nickel based superalloy at different temperatures. *Mater. Sci. Eng. A* **2014**, *599*, 196–203. [[CrossRef](#)]
32. Yu, D. Modeling high-temperature tensile deformation behavior of AZ31B magnesium alloy considering strain effects. *Mater. Des.* **2013**, *51*, 323–330. [[CrossRef](#)]
33. Sakai, T.; Belyakov, A.; Kaibyshev, R.; Miura, H.; Jonas, J.J. Dynamic and post-dynamic recrystallization under hot, cold and severe plastic deformation conditions. *Prog. Mater. Sci.* **2014**, *60*, 130–207. [[CrossRef](#)]
34. Biswas, S.; Beausir, B.T.; Toth, L.S.; Suwas, S. Evolution of texture and microstructure during hot torsion of a magnesium alloy. *Acta Mater.* **2013**, *61*, 5263–5277. [[CrossRef](#)]
35. Kovarik, L.; Unocic, R.R.; Li, J.; Sarosi, P.; Shen, C.; Wang, Y.; Mills, M.J. Microtwinning and other shearing mechanisms at intermediate temperatures in Ni-based superalloys. *Prog. Mater. Sci.* **2009**, *54*, 839–873. [[CrossRef](#)]

36. Zong, Y.; Wen, D.; Liu, Z.; Shan, D.  $\gamma$ -Phase transformation, dynamic recrystallization and texture of a forged TiAl-based alloy based on plane strain compression at elevated temperature. *Mater. Des.* **2016**, *91*, 321–330. [[CrossRef](#)]
37. Xu, S.; Liu, T.; Ding, X.; Zeng, W. Reducing the anisotropy of a pre-twinned hot-rolled Mg–3Al–1Zn alloy by plane-strain compression. *Mater. Sci. Eng. A* **2014**, *592*, 230–235. [[CrossRef](#)]
38. Cheng, L.; Xue, X.; Tang, B.; Liu, D.; Li, J.; Kou, H.; Li, J. Deformation behavior of hot-rolled IN718 superalloy under plane strain compression at elevated temperature. *Mater. Sci. Eng. A* **2014**, *606*, 24–30. [[CrossRef](#)]
39. Uranga, P.; Gutiérrez, I.; López, B. Determination of recrystallization kinetics from plane strain compression tests. *Mater. Sci. Eng. A* **2013**, *578*, 174–180. [[CrossRef](#)]
40. Chen, X.; Lin, Y.C.; Wen, D.; Zhang, J.; He, M. Dynamic recrystallization behavior of a typical nickel-based superalloy during hot deformation. *Mater. Des.* **2014**, *57*, 568–577. [[CrossRef](#)]
41. Yoon, J.G.; Jeong, H.W.; Yoo, Y.S.; Hong, H.U. Influence of initial microstructure on creep deformation behaviors and fracture characteristics of Haynes 230 superalloy at 900 °C. *Mater. Charact.* **2015**, *101*, 49–57. [[CrossRef](#)]
42. Semiatin, S.L.; Weaver, D.S.; Kramb, R.C.; Fagin, P.N.; Glavicic, M.G.; Goetz, R.L.; Frey, N.D.; Antony, M.M. Deformation and recrystallization behavior during hot working of a coarse-grain, nickel-base superalloy ingot material. *Metall. Mater. Trans. A* **2004**, *35*, 679–693. [[CrossRef](#)]
43. Na, Y.S.; Yeom, J.T.; Park, N.K.; Lee, J.Y. Simulation of microstructures for Alloy 718 blade forging using 3D FEM simulator. *J. Mater. Process. Technol.* **2003**, *141*, 337–342. [[CrossRef](#)]
44. Wang, J.; Liu, D.; Hu, Y.; Yang, Y.; Zhu, X. Effect of Grain Size Distribution on Processing Maps for Isothermal Compression of Inconel 718 Superalloy. *J. Mater. Eng. Perform.* **2016**, *25*, 677–686. [[CrossRef](#)]
45. Muralidharan, G.; Thompson, R.G. Effect of second phase precipitation on limiting grain growth in alloy 718. *Scr. Mater.* **1997**, *36*, 755–761. [[CrossRef](#)]
46. Monajati, H.; Taheri, A.K.; Jahazi, M.; Yue, S. Deformation characteristics of isothermally forged UDIMET 720 nickel-base superalloy. *Metall. Mater. Trans. A* **2005**, *36*, 895–905. [[CrossRef](#)]
47. Song, K.; Aindow, M. Grain growth and particle pinning in a model Ni-based superalloy. *Mater. Sci. Eng. A* **2008**, *479*, 365–372. [[CrossRef](#)]
48. Jin, Y.; Bernacki, M.; Agnoli, A.; Lin, B.; Rohrer, G.S.; Rollett, A.D.; Bozzolo, N. Evolution of the Annealing Twin Density during  $\delta$ -Supersolvus Grain Growth in the Nickel-Based Superalloy Inconel™ 718. *Metals* **2016**, *6*, 5. [[CrossRef](#)]
49. Allain, S.; Chateau, J.P.; Bouaziz, O.; Migot, S.; Guelton, N. Correlations between the calculated stacking fault energy and the plasticity mechanisms in Fe–Mn–C alloys. *Mater. Sci. Eng. A* **2004**, *387*, 158–162. [[CrossRef](#)]
50. Randle, V. Twinning-related grain boundary engineering. *Acta Mater.* **2004**, *52*, 4067–4081. [[CrossRef](#)]
51. Wu, K.; Liu, G.Q.; Hu, B.F.; Wang, C.Y.; Zhang, Y.W.; Tao, Y.; Liu, J.T. Effect of processing parameters on hot compressive deformation behavior of a new Ni–Cr–Co based P/M superalloy. *Mater. Sci. Eng. A* **2011**, *528*, 4620–4629. [[CrossRef](#)]
52. Dehmas, M.; Lacaze, J.; Niang, A.; Viguier, B. TEM Study of High-Temperature Precipitation of Delta Phase in Inconel 718 Alloy. *Adv. Mater. Sci. Eng.* **2011**, *2011*, 123–126. [[CrossRef](#)]
53. El-Danaf, E.; Kalidindi, S.R.; Doherty, R.D. Influence of grain size and stacking-fault energy on deformation twinning in fcc metals. *Metall. Mater. Trans. A* **1999**, *30*, 1223–1233. [[CrossRef](#)]

